



Full Text View

[Volume 30, Issue 6 \(June 2000\)](#)

Journal of Physical Oceanography

Article: pp. 1232–1244 | [Abstract](#) | [PDF \(677K\)](#)

Microstructure Observations of Turbulent Mixing in a Partially Mixed Estuary. Part I: Dissipation Rate

Hartmut Peters

Rosenstiel School of Marine and Atmospheric Science, University of Miami, Miami, Florida

Reinoud Bokhorst

RAET IT-Services B.V., Nieuwegein, Netherlands

(Manuscript received June 3, 1998, in final form July 2, 1999)

DOI: 10.1175/1520-0485(2000)030<1232:MOOTMI>2.0.CO;2

ABSTRACT

Variations of turbulent mixing in the water column and in the benthic boundary layer were observed with a microstructure profiler in the Hudson River estuary during two cruises in summer and fall of 1995. Variability patterns of stratification, shear, Richardson number (Ri), and turbulent dissipation rates (ϵ) were similar to those of earlier observations, with strong turbulence in the weakly stratified bottom layer, weak turbulence in the halocline during neap tides, and low Ri and high ϵ spanning the water column during spring ebbs.

Depth-integrated turbulent dissipation rates $\int \rho \epsilon dz$ approximately equaled the work done by the tidal pressure gradient force adjusted for the change in tidal kinetic energy. Alternatively, a suitable scaling for $\int \rho \epsilon dz$ is also provided by the product of bottom shear stress and depth-average velocity $\tau_b \bar{v}$, a

relationship that fails at slack tide, however. At heights above bottom of $z \lesssim 0.3$ m, and again excepting slack tides, observed ϵ were highly correlated with a law-of-the-wall dissipation rate $\epsilon_b = u_*^3 / (\kappa z)$. Ratios ϵ / ϵ_b were close to 1.

Here, the friction velocity is u_* , and von Kármán's constant is κ . Most profiles of the normalized dissipation rate ϵ / ϵ_b showed a weak increase with z in the

lowest 1.5 m, a departure from law of the wall scaling attributed to stable stratification. Such deviations from the law of the wall were smallest during spring floods when the near-bottom stratification was weak or unstable.

Turbulence in the stratified water column well above the bottom appeared to be locally generated by shear instability even though ϵ_b and ϵ were correlated throughout the water column. During spring ebbs, ϵ exceeded ϵ_b by almost an order of magnitude at $z \gtrsim 2$ m.

Table of Contents:

- [Introduction](#)
- [Observations](#)
- [Environmental conditions](#)
- [Typical variability patterns](#)
- [Scaling of dissipation](#)
- [Estuarine energy budget](#)
- [Turbulence above the](#)
- [Summary](#)
- [REFERENCES](#)
- [FIGURES](#)

Options:

- [Create Reference](#)
- [Email this Article](#)
- [Add to MyArchive](#)
- [Search AMS Glossary](#)

Search CrossRef for:

- [Articles Citing This Article](#)

Search Google Scholar for:

- [Hartmut Peters](#)
- [Reinoud Bokhorst](#)

1. Introduction

According to the classical papers on the circulation of estuaries from the 1950s and 1960s (e.g., [Pritchard 1952, 1954, 1956](#); [Rattray and Hansen 1962](#); [Cameron and Pritchard 1963](#); [Hansen and Rattray 1965](#); [Pritchard 1967](#)), turbulent mixing across the halocline is an integral part of the estuarine dynamics to lowest order. Yet, until [Peters \(1997, henceforth referred to as P97\)](#), systematic field measurements of estuarine mixing that resolved its depth–time variability had not been carried out. Analyzing the first of a series of microstructure cruises in the Hudson River, P97 describes a variability pattern of the turbulence in which the tidally driven mixing was always strong in the weakly stratified bottom layer, weak in the halocline during neap tides, and strong across the entire water column during spring ebbs. During the latter, the estimated vertical turbulent salt flux had a typical magnitude of $0.001 \text{ kg m}^{-2} \text{ s}^{-1}$. If it existed in isolation, this flux would have eliminated the haline stratification on a timescale of 4 hours. These observations thus quantitatively confirm the importance of mixing across the estuarine halocline.



This is the first of two companion papers analyzing profiling microstructure observations from the HUDMIX Experiment in the Hudson River estuary in August–October 1995. The experiment was designed to quantify the turbulent transports of momentum and salt and to relate them to local and estuary-wide dynamical balances. The basic objective is to analyze how estuarine mixing arises and how it influences the overall estuarine dynamics. This paper analyzes the variability of turbulent dissipation rates, while the companion paper ([Peters and Bokhorst 1999](#), manuscript submitted to *J. Phys. Oceanogr.*, henceforth referred to as Part II) discusses the magnitude and depth–time variation of the vertical turbulent salt flux and turbulent stress.

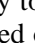

The conceptual idea behind the HUDMIX Experiment is that estuarine mixing is essentially a boundary layer process driven by the local bottom shear stress rather than resulting from internal shears independent of the bottom forcing. This is not meant to imply that all turbulent kinetic energy is derived from bottom friction but rather that shear is set up throughout the water column because of the presence of bottom friction. Hence this concept is compatible with [Geyer and Smith's \(1987\)](#) notion of turbulence in highly stratified estuaries being generated by local shear instabilities in the water column as well as with [Trowbridge's \(1992\)](#) appealingly simple, yet successful, model of boundary layers extending into stratified flows via shear instability. In contrast, [Jay and Smith \(1990a\)](#) suggested that mixing in partially mixed estuaries arises from random internal waves. This paper provides evidence for the validity of [Geyer and Smith's \(1987\)](#) concept.

The observations and environmental conditions relevant to the analysis, river discharge, atmospheric forcing, and tidal amplitudes, are outlined in [sections 2](#) and [3](#), respectively. [Section 4](#) contains a summary of the typical variability patterns of turbulent mixing and tidal flow. Thereafter, we discuss the magnitude and scaling of dissipation rates in relation to the estuarine energy budget ([sections 5](#) and [6](#)). The generation of turbulence in the water column above the bottom boundary layer, taken as the constant stress layer, is analyzed in [section 7](#). The paper concludes with a summary and a brief discussion.

2. Observations

a. The 1995 HUDMIX Experiment

During HUDMIX, we took microstructure measurements during 11½ days as shown in [Fig. 1](#) . The first survey took place in August, referred to as cruise HUDM1, and the second in October, cruise HUDM2. On most days, we measured over the duration of a semidiurnal tidal cycle with some gaps resulting from instrumental problems and logistical constraints. Both cruises covered neap tides and spring tides, and comprised 1250 and 1095 microstructure profiles, respectively, which we also call drops. In [Fig. 1](#)  and throughout this paper, yeardays are labeled at 0000 Universal Time (UTC, 1900 Eastern Standard Time on the previous day). Following tradition, the first of January is yearday 1, such that day 229 is 17 August 1995 and day 291 is 18 October.

In addition to our own microstructure measurements, we use part of the concurrent observations made by [Geyer et al. \(2000\)](#) and [Trowbridge et al. \(1999\)](#). These include (i) measurements of turbulent velocity, salinity, and temperature from a bottom quadrupod with Benthic Acoustic Stress Sensors (BASS) at a central site marked in [Fig. 2](#) ; (ii) velocity and stratification measurements with a moored 1200-kHz narrowband upward-looking acoustic Doppler current profiler (ADCP) and moored Seacat CT recorders close to the BASS site; (iii) bottom-mounted moorings with velocity, temperature, salinity, and pressure recorders along both sides of the river spanning a 6-km stretch centered on the BASS/ADCP site; (iv) alternating across-river (spanwise) and along-river (streamwise) CTD surveys made with a fast small boat; and (v) meteorological measurements (located on the Manhattan shore at $y = 2.7 \text{ km}$ in [Fig. 2](#) .

The site of the experiment (Fig. 2) was chosen in a geometrically relatively uniform stretch of the estuary with strong tides, persistent stratification, and strong residual circulation. Attempting to possibly find the classical estuarine circulation, as referenced in the introduction, we tried to avoid complex flow processes related to internal hydraulics, secondary flows, etc., as much as possible. Such processes occur in the Hudson Estuary, for example, in the vicinity of the George Washington Bridge (located at $y \approx 12$ km in Fig. 2) (Chant and Wilson 1997).

For convenience, we use a Cartesian coordinate system with origin at 40.75°N , 74°W and y axis pointing toward 30° true, the direction of the local river axis. In these coordinates, The Battery at the southern tip of Manhattan, river mile 0, is at $y \approx -5.5$ km.

b. Instrumentation

Our measurements include profiles from a ship-mounted 600-kHz broadband ADCP and from the loosely tethered shallow water microstructure profiler (SWAMP, introduced in P97). Measured data consist of Sea-Bird CTD channels for pressure (p), temperature (T), and conductivity (converted to salinity, S), microstructure shear fluctuations from shear probes, microstructure temperature from a fast thermistor, and microstructure conductivity from a Sea-Bird dual needle probe. Auxiliary sensors include two inclinometers and one accelerometer. Most drops cover the benthic boundary layer to a height of 15 cm above the bottom. Unlike during an earlier cruise (P97), we operated SWAMP from the drifting ship for technical reasons. Observations were thus taken over a $2 \text{ km} \times 0.5 \text{ km}$ area centered around the central moorings (Fig. 2). Even though temporal and spatial variations are mixed in our measurements, we were still essentially observing temporal variations at tidal and subtidal frequencies as shown below. Geyer et al. (2000) argue that the spatial averaging provided by our microstructure profiling had some advantages over fixed point measurements with respect to integral estuarine energy, momentum, and mass budgets.

The measured microstructure shear allows computing the viscous dissipation rate ϵ under the assumption of isotropy while separating signal and instrumental noise in the spectral domain. We describe in Part II how eddy viscosity, eddy diffusivity, and turbulent fluxes of momentum and salt can be estimated from ϵ and vertical velocity and salinity gradients. The microstructure conductivity and temperature serve to determine turbulent overturning scales following Thorpe (1977).

c. Reduction and validation of microstructure data

Peters (1997) and references cited therein describe the reduction of microstructure data, information not repeated here for the sake of brevity. We note, however, that ϵ often was very large such that the viscous range of the shear spectrum was not resolved and that ϵ was essentially determined from the inertial subrange. We further refer to Lueck et al. (1997) with respect to problems and uncertainties of dissipation measurements. One additional comment concerns a worrisome aspect of microstructure measurements, contaminations by platform vibration and waterborne objects colliding with the shear probes. The latter include suspended sediment particles, which are inevitably present in energetic estuaries, especially near the bed, and objects as mundane as plastic bags. Even after using accelerometer data to detect problems like cable strumming, eliminating sections of gross mismatch between the two shear probe signals, and clipping large spikes in ϵ , a few contaminated data segments still needed to be removed manually.

A comparison of our ϵ with dissipation rates computed from the fixed-point BASS measurements of Trowbridge et al. (1999) shows a high level of consistency between the two independent datasets. The two sets of ϵ from $2.08 \leq z \leq 2.73$ m are highly correlated (correlation coefficient 0.85 in 1-h averages from HUDM2), and their magnitudes agree to within 30% on average despite profound differences in sampling. Trowbridge et al. (1999) determined ϵ from fitting the inertial subrange of velocity spectra, a procedure compatible with our approach (see above).

d. Averaging

Turbulent dissipation rates need to be averaged in order to achieve reasonable statistical confidence levels given their approximately lognormal distributions (e.g., Yamazaki and Osborn 1993). We compute averages along constant normalized depth z/H , where z is height above bottom and H is the local water depth at each drop, and in bins of the M_2 tidal phase ϕ_{M_2} . The latter is determined by means of complex demodulation of the water-level data from The Battery. The water level is represented as

$$\zeta(t) = a(t) \cos[\omega_{M_2} t + \phi(t)] + n(t) = a(t) \cos[\phi_{M_2}(t)] + n(t), (1)$$

with slowly varying amplitude $a(t)$ and phase $\phi(t)$. Variations with frequencies much higher and lower than $\omega_{M_2} = 2\pi/12.4$ h are contained in $n(t)$. The demodulation is carried out with a filter wide enough to pass both M_2 and S_2 tides. Time t

assigns phases $\phi_{M2}(t)$ to ADCP and profiler data. Depth-averaged streamwise currents are displayed as function of Φ_{M2} in [Fig. 3](#), which shows that flood is equivalent to $270^\circ < \phi_{M2} \leq 360^\circ$ and $0^\circ \leq \phi_{M2} < 90^\circ$, while $90^\circ < \phi_{M2} < 270^\circ$ corresponds to ebb.

Averages along normalized depth approximately preserve the structure of both top and bottom boundary layers. In order to analyze the benthic boundary layer, the height above bottom needs to be known very accurately. We determined both z and H from the pressure reading at the bottom impact recorded by the accelerometer of SWAMP; the precision is about 0.03 m.

3. Environmental conditions and tides

a. River discharge

Naturally, the stratification of estuaries is affected by the river flow. The actual discharge of the Hudson River, shown in [Fig. 4](#), deviated from the climatology in relationship to the 1995 drought that ended with heavy precipitation on 21–22 October 1995 (1995 yeardays 294–295). The associated storm caused significant variations in flow and stratification at Manhattan as mentioned below. The river flow at Green Island near Albany, New York, is representative of the flow at The Battery, Manhattan, 245 km downstream, because tributary discharges are small ([Abood 1977](#)) Discharge variations propagate over that distance in about 7 h.

b. Tides

Because tidal currents in the Hudson River exceed residual currents by an order of magnitude, as seen, for example, in our own observations, turbulence is dominantly generated by tidal shear. Correspondingly, our cruises were designed to capture the neap-to-spring transition of flow, stratification, and mixing ([Haas 1977](#); [Jay and Smith, 1990b](#); [Geyer and Cannon 1982](#)). The increase in semidiurnal tidal amplitude from neaps to springs was modest during HUDM, but much stronger during HUDM2 ([Figs. 3](#) and [1](#)). The latter shows that the amplitude of the water level at The Battery, ζ_{ampl} , and the amplitude of depth-averaged currents from our shipborne ADCP, v_{ampl} , were well correlated. Herein, the along-river, streamwise, current component is denoted as v .

c. Local and remote atmospheric forcing

The local atmospheric surface forcing by solar radiation and wind was mostly unimportant during our experiment, exceptions not being relevant to our analysis. Observed temperature variations, affected by the local solar heat input, were too small to significantly modify the saline stratification, and the surface wind stress was generally small compared to tidal stresses. This can easily be seen by comparing the *maximum* wind speeds of 10 m s^{-1} ([Figs. 4e,j](#)), corresponding to a surface wind stress of about 0.1 Pa, with a *typical* tidal velocity of 1 m s^{-1} ([Fig. 3](#)), corresponding to a bottom stress of about 1 Pa.

Unlike local atmospheric forcing, regional forcing strongly affected the estuarine flow. The storm of yearday 294, already mentioned above, is seen as a strong drop in atmospheric pressure, p_a , in [Fig. 4h](#), which corresponds to a rise in water level at The Battery depicted in [Fig. 1e](#). This change in water level was most likely related to the changing atmospheric pressure directly through the inverted barometric effect and indirectly through the regional wind stress over the New York Bight resulting in water level variations at the mouth of the estuary. The rise in water level at The Battery corresponded to inflow into the estuary, and the fall to outflow as seen in [Fig. 4h](#), which displays p_a as well as the depth-averaged, low-passed moored ADCP current measurements.

The low-passed flow was also affected by the surge in river discharge at Green Island shown in [Fig. 4g](#). A flow rate of $1400 \text{ m}^3 \text{ s}^{-1}$ corresponds to a mean velocity of about 0.1 m s^{-1} at the central mooring, a significant fraction of the observed depth-averaged flow. Net outflow is also seen in our shipborne ADCP observations on yeardays 295–296 ([Fig. 3b](#)). Note the downward shift of the corresponding traces relative to those from the previous days.

4. Typical variability patterns of flow and mixing

The depth–time variability of along-river velocity, salinity, gradient Richardson number, Ri , and viscous dissipation rate is displayed in [Fig. 5](#) for one day representative of neap conditions and spring conditions, each, from HUDM2. Velocity and salinity show the expected increase in currents and decrease in stratification upon the progression from neap to spring tides. Our observations also show the expected ebb–flood asymmetry related to the straining of the streamwise salinity gradient by

the tidal and residual flow (Simpson et al. 1990). Note that vertical shear was approximately constant with depth during ebb, while a jet appeared on flood that migrated from the bottom toward the surface.

Low-gradient Richardson numbers appeared throughout the water column on spring ebbs, while they were otherwise restricted to the weakly stratified bottom layer. In apparent response to Ri , turbulent dissipation rates were always large in the weakly stratified bottom layer except on slack tides (Figs. 5d,h). They were mostly weak in the halocline during neaps, while high ϵ spanned the whole water column during spring ebbs. Spring conditions of HUDM2 showed a pronounced ebb–flood asymmetry in mixing, dissipation rates being larger higher above the bottom during ebb than during flood. Even though the flood phase of 22 October was not completely covered by our measurements, the other days of spring tide of HUDM2, 21 and 23 October, confirm the asymmetry. The ebb–flood asymmetry was weak during the springs of HUDM (not shown).

The onset of low Ri and high ϵ during spring ebbs shows a delay with increasing height above the bottom that spans about 2 h (Figs. 5g,h). This feature appears to be a robust property of estuarine tidal flow as it was already seen during the 1994 “HUD1” cruise (P97). The pattern gives the appearance of “mixing working its way up from the bottom.” The low Ri of spring ebbs results from a combination of high shear and low N^2 (not shown; see P97). The low N^2 is in contrast to the tendency of advection during ebb to increase stratification by differentially moving fresher water over salty water. The likely cause for the decrease in N^2 during spring ebb thus is mixing, Part II showing that the turbulent salt flux was large enough to significantly affect the stratification.

The observations shown in Fig. 5 closely resemble their counterparts from the May 1994 cruise HUD1 analyzed in P97. Hence, the variability patterns of estuarine flow and mixing described in P97 appear to be quite repeatable.

It is obvious that variability in the contoured flow variables of Fig. 5 is dominated either by the semidiurnal tidal period or, in the case of the positive definite variable ϵ , at quarterdiurnal and semidiurnal periods. Essentially, we observed temporal variations even though the measurements were not taken at a fixed location, unlike during HUD1, when the ship was moored. Temporal fluctuations in flow and mixing dominate in our observations at tidal frequencies because our observations were taken mostly within ± 1 km of the central moorings, while the streamwise tidal excursion is much larger, about ± 7 km. An inspection of our data at higher resolution than in Fig. 5 shows that variations at periods shorter than semidiurnal were indeed affected by spatial gradients.

The averages displayed in Fig. 5 were computed over 20° bins in M_2 phase, or over about 40 min. Except for one empty bin, the number of microstructure drops in each bin varied between 4 and 25, the average being 12.

5. Scaling of dissipation rates

a. Scaling of ϵ in the bottom boundary layer

Most of our microstructure profiles reach to within $z = 0.15$ m of the bottom, and thus we can examine the structure of the boundary layer, taken to be the constant stress layer typically 1 m thick following Trowbridge et al. (1999). We analyze dissipation rates scaled by the friction velocity u_* and, in the course of this analysis, we also gain some hints concerning the systematic uncertainty of ϵ .

The theory of neutrally stratified boundary layers predicts that dissipation rates in the constant stress layer are related to

$$u_* = \sqrt{\tau_b/\rho} \quad \text{as} \quad (2)$$

$$\epsilon_b = u_*^3 (\kappa z)^{-1}. \quad (3)$$

Here, $\kappa = 0.4$ is von Kármán’s constant and τ_b is the magnitude of the bottom shear stress


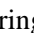



$$\tau_b = \rho c_d |\mathbf{u}_b| \mathbf{u}_b. \quad (4)$$

The latter is computed from ADCP velocity data collocated with the microstructure drops using 6-min averages to suppress noise. Hence, u_* and ϵ are completely independent. The assumed drag coefficient $c_d = 0.002$ was applied to the velocity vector \mathbf{u}_b from the lowest ADCP bin, typically 2.25 m above the bottom, that is, well above the constant stress layer. A roughness length of 0.001 m was used to adjust the drag coefficient to the height of the lowest ADCP bin. The drag coefficient and roughness length are based on Trowbridge et al. (1999), who found systematic variations in wall layer scaling as a function of z . Because of these variations, the assumed drag coefficient may be uncertain by possibly 25%.

Excluding data from slack tides, normalized dissipation rates ϵ/ϵ_b at $z = 0.275$ m were approximately lognormally distributed around median values of 0.8–0.9 with arithmetic means of 1.35–1.42. These ϵ were thus consistent with boundary layer scaling. During slack tides, however, when the bottom shear stress was small, $\tau_b \lesssim 0.1$ Pa, ϵ tended to be significantly larger than ϵ_b . This departure from boundary layer scaling may have been related to significant stratification even very close to the bottom and to large turbulence timescales during slack tides as discussed below.

Our comparison of ϵ and ϵ_b is based on work of [Dewey et al. \(1987\)](#) and [Dewey and Crawford \(1988\)](#), who first estimated the bottom shear stress from profiles of near-bottom dissipation rates. Statistical confidence limits were evaluated by [Crawford and Dewey \(1990\)](#). The spread of distributions of ϵ/ϵ_b in our observations is compatible with their results. Standard deviations of the natural logarithm of ϵ/ϵ_b ranged from 0.8 to 1.2.

b. Structure of the boundary layer

Scaled dissipation rates ϵ/ϵ_b tended to increase with z except during spring floods ([Fig. 6](#) ). The magnitude of this trend varied considerably among different tidal cycles, and scatter is apparent. However, the repeated occurrence of the trend in a number of datasets lends it credibility. We attribute the increase of ϵ/ϵ_b with z to the effect of stable stratification, which often reached very close to the bottom as in the example of [Fig. 7](#) . In contrast, spring floods tended to have the weakest stratification in general, and unstable stratification near the bottom. The latter occurs because flood currents increasing with z above the bottom ([Fig. 5](#) ) differentially advect heavier water over lighter water. [Figure 6d](#)  shows that during spring floods boundary layer scaling $\epsilon \approx \epsilon_b$ held over the lowest 1.5 m above the bottom. The different traces in [Fig. 6](#)  are from different days, data from near slack tides have been excluded.

c. Depth-integrated dissipation rates

Despite the pronounced and complex depth–time variability of ϵ summarized in [section 4](#), a simple scaling relationship for depth-integrated dissipation rates can be derived for one-dimensional steady channel flow. In such flow, assuming a production–dissipation balance of turbulent kinetic energy (TKE), a no-slip condition at the bottom, and a negligibly small surface stress, we can simplify the TKE equation to

$$\int_0^H \rho \epsilon \, dz \approx \int_0^H \tau \frac{\partial v}{\partial z} \, dz = - \int_0^H v \frac{\partial \tau}{\partial z} \, dz. \quad (5)$$


Here, ρ is density, and τ is the depth-dependent turbulent stress. This expression is to be combined with the linearized momentum balance in the streamwise direction,

$$\rho \frac{\partial v}{\partial t} = \frac{\partial p}{\partial y} + \frac{\partial \tau}{\partial z}. \quad (6)$$

We assume steady state and neglect the baroclinic part of the pressure gradient such that $\partial p/\partial y$ and consequently $\partial \tau/\partial z$ become independent of z . Thereafter, the integral on the right-hand side of [\(5\)](#) can be executed, and the desired scaling is found as

$$\int_0^H \rho \epsilon \, dz = \bar{v} \tau_b \equiv W_b. \quad (7)$$

The right-hand side is the product of depth-averaged velocity and bottom shear stress. In tidal flows, the local rate of change $\rho \partial v/\partial t$ in [\(6\)](#) and the storage of TKE are not small, and thus it is not trivial that [\(7\)](#) provides a suitable scaling for depth-integrated dissipation rates in unsteady tidal regimes. It is tempting to test the relationship because the right-hand side of [\(7\)](#) can be obtained comparatively easily from ADCP measurements alone.

[Figure 8](#)  shows that $\int \rho \epsilon \, dz$ followed W_b over nearly two decades of variability at $W_b \gtrsim 5 \times 10^{-2} \text{ W m}^{-2}$. The similarity of $\int \rho \epsilon \, dz$ and W_b held during most ebbs and floods and during spring and neap tides (not specifically shown),

but it generally failed around slack tide when v ranged within $\pm 0.2 \text{ m s}^{-1}$. Further mismatch of W_b and $\int \rho \epsilon dz$ occurred in a small number of ebb data with depth-average speeds of -0.3 to -0.5 m s^{-1} and an even smaller number of flood data.

It is important to realize that depth-integrated dissipation rates predominantly originate from the bottom boundary layer. Even before the lowest 0.15 m not covered by our measurements are accounted for, 50% of the cruise average $\int \rho \epsilon dz$ originate from the lowest 2.5 m (not shown, but see [Fig. 5](#)). Hence, dissipation within the shear flow well above the bottom was relatively small.

Our microstructure profiles neither cover the lowest 15 cm near the bottom nor the the upper ~ 3 m. [Figure 8](#) has not been corrected for these omissions. Omitting the near-surface region is a minor problem because the wind stress was much smaller than the tidally driven bottom stress (except during slack tides). However, omitting the lowest 0.15 m leads to a significant underestimate in $\int \rho \epsilon dz$ owing to ϵ varying like z^{-1} in the boundary layer. With roughness length $z_0 = 0.001 \text{ m}$ as above, and assuming hydrodynamically rough flow, an upper bound to the underestimate can be found as $\int_{z_0}^{\infty} z^{-1} dz / \int_{z=0.15\text{m}}^{\infty} z^{-1} dz \approx 3.6$. The assumed roughness length of 1 mm appears rather small. If it had been larger, the true underestimate of $\int \rho \epsilon dz$ would have been smaller than a factor of 3.6. The latter is indicated by an analysis of the estuarine energy budget given below.

d. Slack tide

We find that depth-integrated dissipation rates were much larger than W_b during slack tides ([Fig. 8](#)). A consideration of the characteristic dissipative timescale of the turbulence shows that the unsteadiness of the TKE balance cannot be neglected near slack tides. While ϵ scales like (3), the near-bottom TKE, k , scales like $k \sim u_*^2$. The timescale τ_ϵ thus varies like $\tau_\epsilon = k/\epsilon \sim u_*^{-1} z$. With $u_*^{-1} \rightarrow \infty$ as $u_* \sim u \rightarrow 0$, the timescale becomes large near slack tide, and the turbulence can effectively be sustained by the existing TKE.

We further suspect that the weak but nonzero mixing near slack tide was related to baroclinic processes such as internal waves and gravity currents. During spring tides, we observed inversions in temperature profiles that may have been generated by adjustment under gravity related to spanwise and streamwise density differences created during strong tidal flow and mixing. This topic still awaits exploration.

6. Estuarine energy budget

Relationships between viscous dissipation and work done by the tidal pressure gradient force developed in [section 5](#) can be extended to the unsteady case. Inserting (6) into (5) yields

$$\int_0^H \rho \epsilon dz \approx \int_0^H v \left(-\frac{\partial p}{\partial y} - \rho \frac{\partial v}{\partial t} \right) dz. \quad (8)$$

Depth-integrated dissipation equals pressure gradient work minus change of kinetic energy. In the following, we refer to the right-hand side of (8) as “net tidal work.”

We apply (8) to HUDM2 observations using moored measurements of the streamwise barotropic pressure gradient and, for simplicity, using depth-averaged velocities v from the central ADCP mooring. The right-hand side of (8) is approximated as $Hv(-\partial p/\partial x - \rho \partial u/\partial t)$ with $H = 15 \text{ m}$. This simplification appears justified given that the baroclinic pressure gradient is neglected and that pressure gradient, tidal velocity, and $\int \rho \epsilon dz$ were each sampled in a different way. [Figure 9](#) demonstrates that depth-integrated dissipation and net tidal work tracked each other well at least during spring tide. The graph displays $2.5 \times \int \rho \epsilon dz$, the factor of 2.5 approximately correcting for dissipation in the lowest 15 cm above the bottom not covered by our profiles (see above). Hence, the observed depth-integrated dissipation rates approximately equaled the work done by the tidal pressure gradient force adjusted for the change in kinetic energy, indicating a rough closure of the integral energy budget.

The 2-h averages of $2.5 \times \int \rho \epsilon dz$ shown in [Fig. 9](#) and the net tidal forcing are significantly correlated with Pearson correlation coefficient of 0.78 (Spearman’s rank order coefficient 0.62). The slope of a symmetrical least squares fit of $\int \rho \epsilon dz$ as function of net tidal work is 0.32 with confidence bounds [0.22, 0.44]. Using individual drops instead of 2-h

averages produces a larger slope of 0.42. These slopes are compatible with factors of 2.3–3.1 correcting for omitted dissipation in the lowest 15 cm.

The symmetrical fit minimizes the sum of squared distances from the data points orthogonally to the regression line. Analytical expressions for confidence limits of the fit parameters are unavailable to our knowledge; we find them through bootstrapping (Efron and Gong, 1983). Ordinary linear fits produce conflicting results depending on whether net tidal work or $\int \rho \epsilon dz$ is considered the independent variable.

Observed $\int \rho \epsilon dz$ and W_b were systematically smaller than net tidal work during neap ebbs when the barotropic and the neglected baroclinic pressure gradients opposed each other (days 291 and 293 in Fig. 9). The baroclinic pressure gradient can be inferred from along-river CTD sections showing $\partial\rho/\partial y \approx -2.2 \times 10^{-4} \text{ kg m}^{-4}$ during HUDM2 neap tides. The corresponding middepth baroclinic pressure gradient is -0.016 Pa m^{-1} , much smaller than the barotropic pressure gradient of the order of 0.1 Pa m^{-1} . Thus it appears that the omitted baroclinic pressure gradient cannot account for the deficit in the energy balance during neap ebbs.

7. Turbulence above the bottom boundary layer

After having analyzed depth-integrated as well as near-bottom dissipation rates, we now discuss turbulence above the bottom boundary layer, which we take as the constant stress layer of a typical thickness of about 1 m or less (Trowbridge et al. (1999)). For the patterns of variability of ϵ , we refer to section 4. As an alternative to the contours of Fig. 5, we display average ϵ as a function of tidal phase, depth, and progress from neap to spring tides as simple line diagrams in Fig. 10. While averaging uses normalized depth z/H , the discussion is in terms of nominal dimensional depth assuming a mean water depth of 16.2 m. Depth bins of 2.7-m thickness are located on average at $z = 5.4, 8.1, 10.8 \text{ m}$. Thus even the lowest depth bin is outside of the constant stress layer. The size of phase bins is 30° for 18–19 and 22–23 October, and 45° for 20–21 October. Figure 10 depicts statistical confidence limits based on bootstrapping (Efron and Gong 1983) at the 97% confidence level. Simple numerical experiments show that, for normally distributed data, bootstrapping at the 97% level produces about the same confidence intervals as parametric estimates at the 95% confidence level. It is apparent from Fig. 10 that statistical uncertainties in ϵ are small compared to the dominant tidal variability.

It is instructive to compare the actual ϵ with the law-of-the-wall ϵ_b of (3). Figure 10 displays a considerable degree of correlation and similarity of magnitudes of ϵ and ϵ_b throughout cruise HUDM2 even far from the bottom in significant stratification. The correlation coefficient of ϵ and ϵ_b from the entire cruise at $z = 10.8 \text{ m}$ (8.1 m) is 0.56 (0.66). Large deviations with $\epsilon \gg \epsilon_b$ occurred near slack tides and during spring tide ebb, when ϵ exceeded ϵ_b by factors of 5–10 throughout the water column (Figs. 10g–i).

a. Shear instability

Taken to the extreme, the degree of correspondence between ϵ and ϵ_b shown in Fig. 10 could suggest that TKE throughout the water column was essentially exported from the bottom. We now show, however, that this was likely not the case and that turbulence well above the bottom was generated locally. This scenario is consistent with a correlation of ϵ and ϵ_b because the local shear and Ri as well as ϵ_b all varied with the semidiurnal tide.

Indications for the importance of local shear instability in the generation of TKE are easily found, for example, in simple plots of dissipation rates versus gradient Richardson number as shown in P97. With critical $Ri \approx 1/4$ (Miles 1961), one expects dissipation rates to increase at $Ri \approx 1/4$, and this is indeed observed. Further evidence for the importance of local shear production is warranted, however. Trowbridge (1992) developed a simple criterion for turbulence being constrained by stratification somewhere in the water column. A bulk Richardson number R_* measures the tendency of stratification to suppress mixing relative to the strength of mixing represented by the bottom shear stress: $R_* = \rho B \tau_b$ with integrated buoyancy anomaly $B = \rho^{-1} g \int_0^H [\rho(z) - \rho(H)] dz$. By comparing internal production of TKE with wall layer theory, $R_*^{-1/4}$ can be interpreted as the ratio of the effective thickness of the wall layer to the water depth. Thus, $R_*^{-1/4} \approx 1$ indicates that the wall layer filled the entire water column.

Data from HUDM2 show $R_*^{-1/4} \approx 0.2$ most of the time except during spring ebbs, especially on day 295 (Fig. 11), when $R_*^{-1/4}$ reached 0.5. Spring floods had moderate $R_*^{-1/4} \approx 0.3$. Section 4 points out that the stratification became very weak during the spring ebb of day 295 (as a result of turbulent mixing as shown in part II), thus explaining the high

value of $R_*^{-1/4}$. The increased stratification of day 296, caused by external forcing as outlined above, corresponded to smaller $R_*^{-1/4}$ than on the previous day. In summary, [Trowbridge's \(1992\)](#) criterion indicates that the wall layer only occupied a fraction of the water column above the bottom except during brief periods of spring tide. As there was turbulence throughout the water column, turbulence above the wall layer must have had a local source of energy related to shear instability.

It is instructive to show an example of turbulent mixing through the water column during spring ebb, when shear and stratification tend to be uniform with depth ([Geyer and Smith 1987](#), P97). We choose one of the more dramatic examples. On 23 October 1995, during strong spring tides, external forcing had reintroduced strong stratification in excess of that on 22 October. [Figure 7](#) shows very high N^2 that reached practically down to the bottom, strong shear, and low Ri. Turbulent displacements ζ_{th} and [Thorpe \(1977\)](#) scales l_{th} show that overturning occurred throughout the water column. At $z > 2.4$ m, ϵ exceeded $\epsilon_b = u_*^3 / (\kappa z)$ by an order of magnitude, and indication of local sources of TKE throughout the water column. The condition $\epsilon \geq 10\epsilon_b$ and the shape of the depth distribution of ϵ are incompatible with generation of turbulence exclusively near the bottom.

[Figure 7](#) does not show a bottom mixed layer, and one should not necessarily expect it to exist. A “mixed layer” requires a weakly stratified and vigorously mixing region near a boundary and a stratified, more quiescent interior of the fluid. In contrast, our example shows stratification, vigorous mixing, and overturning throughout the water column.

8. Summary

Our examination of turbulent dissipation rates in a partially mixed estuary can be summarized as follows.

1. Relative maxima of dissipation rates migrated from occurring during flood on neap tides to ebb on spring tides. Spring ebbs showed the overall highest ϵ of the order of 10^{-4} W kg⁻¹ throughout the water column.
2. At least during spring tides, depth-integrated dissipation rates approximately corresponded to the work done by the tidal pressure gradient force adjusted for the rate of change of mean kinetic energy, indicating an approximate closure of the integral energy budget. Depth-integrated dissipation rates also followed the product of bottom stress and depth-averaged velocity except near slack tides.
3. Close to the bottom, average observed dissipation rates approximately equaled the law-of-the-wall dissipation rate $\epsilon_b = u_*^3 (\kappa z)^{-1}$ except near slack tides.
4. Local ϵ even well above the bottom and in significant stratification showed some correspondence to ϵ_b , but the correspondence was diminished with increasing distance from the bottom. Measured ϵ exceeded ϵ_b during spring ebb throughout the water column above the bottom boundary layer.
5. An analysis relating bottom shear stress to stratification following [Trowbridge \(1992\)](#) and a close examination of individual profiles of stratification, shear, and ϵ indicate the importance of local shear instability in the generation of turbulence above the bottom boundary layer taken to be the constant stress layer.

The scaling of depth-integrated dissipation rates with bottom shear stress times depth-averaged velocity is highly convenient because velocity and stress are easily measured and estimated. Theoretically, it does not hold in unsteady flow, but practically this had little consequence except for slack tides. The correspondence of depth-integrated dissipation rates to net tidal work, the work done by the pressure gradient adjusted for the rate of change of tidal kinetic energy, holds in unsteady flow, but measurements of the streamwise pressure gradient are more difficult and costly than velocity measurements.

The introduction to this paper states the conceptual idea behind our HUDMIX experiment, estuarine mixing being a boundary layer process dominated by the bottom shear stress. While [Geyer et al. \(2000\)](#) confirm this idea in terms of the dynamics of the estuarine, or residual, flow, we look at it in terms of turbulent mixing. Dissipation rates at all depths bear resemblance to the variability of the bottom shear stress, while simultaneously turbulence outside of the bottom boundary layer appears to be locally generated by shear instability. Beyond this, explaining the depth–time variability of dissipation rates off the bottom is much more difficult than explaining depth-averaged dissipation because there is no simple recipe for stratified turbulence, a statement elaborated in Part II. Thus, we have begun to investigate how well turbulence closure models can simulate the observed $\epsilon(z, t)$.

Acknowledgments

The National Science Foundation supported the experiment “Stress, Salt Flux and Dynamics of a Partially Mixed Estuary” (OCE 9415582/99796016), additional funds being granted for the purchase of a broadband ADCP [OCE 9122668, with matching funds provided by the Research Foundation of SUNY and the Marine Sciences Research Center Stony Brook (MSRC)]. The establishment of an estuarine microstructure program would have been impossible without the generous help of a number of researchers in the microstructure field for which we are very grateful. Sincere thanks go especially to Neil Oakey, and to Mike Gregg, Rolf Lueck, Bill Crawford, Ann Gargett, and Jim Moum. The microstructure profiler SWAMP, designed and built by Seimac Ltd, and the winch/line puller system, built by Brooke Ocean Technology, both of Dartmouth, Nova Scotia, went through over 6000 microstructure drops and some 4000 bottom landings at 1 m s^{-1} . Tom Wilson and Mark Wiggins provided expert engineering and technical assistance at MSRC and in the field. Captain Bret Zielinski of the R/V *Onrust* contributed greatly to the success of the measurements, as did participating MSRC students Dave Ullman, Lorraine Heilman, and Chi-Shao Chen. Constructive comments by John Simpson and an anonymous reviewer are greatly appreciated. Last but not least, the continuing collaboration with Rocky Geyer, John Trowbridge, Sandy Williams, and Melissa Bowen of the Woods Hole Oceanographic Institution has been highly enlightening and a true pleasure. They kindly made some of their moored and shipborne measurements available for our analysis.

REFERENCES

- Abood, K. A., 1977: Evaluation of the circulation in partially stratified estuaries as typified by the Hudson River. Ph.D. dissertation, Rutgers University, 422 pp..
- Cameron, W. M., and D. W. Pritchard, 1963: Estuaries. *The Sea: Ideas and Observations on Progress in the Study of the Seas*, Vol. 2, *The Composition of Sea-Water, Comparative and Descriptive Oceanography*, M. N. Hill, Ed., Wiley-Interscience, 306–324..
- Chant, R. J., and R. E. Wilson, 1997: Secondary circulation in a highly stratified estuary. *J. Geophys. Res.*, **102**, 23 207–23 215..
- Crawford, W. R., and R. K. Dewey, 1990: Confidence limits for friction velocity determined from turbulence profiles in coastal waters. *J. Atmos. Oceanic Technol.*, **7**, 50–57..
- Dewey, R. K., and W. R. Crawford, 1988: Bottom stress estimates from vertical dissipation rate profiles on the continental shelf. *J. Phys. Oceanogr.*, **18**, 1167–1177.. [Find this article online](#)
- , —, A. E. Gargett, and N. S. Oakey, 1987: A microstructure instrument for profiling oceanic turbulence in coastal bottom boundary layers. *J. Atmos. Oceanic Technol.*, **4**, 288–297..
- Efron, B., and G. Gong, 1983: A leisurely look at the bootstrap, the jackknife, and cross-validation. *Amer. Stat.*, **37**, 36–48..
- Geyer, W. R., and G. A. Cannon, 1982: Sill dynamics related to bottom water renewal in a fjord. *J. Geophys. Res.*, **87**, 7985–7996..
- , —, and J. D. Smith, 1987: Shear instability in a highly stratified estuary. *J. Phys. Oceanogr.*, **17**, 1668–1679.. [Find this article online](#)
- , —, J. H. Trowbridge, and M. M. Bowen, 2000: The dynamics of a partially mixed estuary. *J. Phys. Oceanogr.*, in press..
- Haas, L. W., 1977: The effects of the spring–neap tidal cycle on the vertical salinity structure of the James, York and Rappahannock Rivers, Virginia, U.S.A. *Estuar. Coastal Mar. Sci.*, **5**, 485–496..
- Hansen, D. V., and M. Rattray Jr., 1965: Gravitational circulation in straits and estuaries. *J. Mar. Res.*, **23**, 104–122..
- Jay, D. A., and J. D. Smith, 1990a: Residual circulation in shallow estuaries. 2: Weakly stratified and partially mixed, narrow estuaries. *J. Geophys. Res.*, **95**, 733–748..
- , —, and —, 1990b: Circulation, density distribution and neap–spring transitions in the Columbia River estuary. *Progress in Oceanography*, Vol. 25, Pergamon, 81–112..
- Lueck, R. G., D. Huang, D. Newman, and J. Box, 1997: Turbulence measurements with a moored instrument. *J. Atmos. Oceanic Technol.*, **14**, 142–161..
- Miles, J. W., 1961: On the stability of heterogeneous shear flow. *J. Fluid Mech.*, **10**, 496–508..
- Peters, H., 1997: Observations of stratified turbulent mixing in an estuary. Neap-to-spring variations during high river flow. *Estuarine*,

Pritchard, D. W., 1952: Estuarine hydrography. *Advances in Geophysics*, Vol. 1, Academic Press, 243–280..

— ,1954: A study of the salt balance in a coastal plain estuary. *J. Mar. Res.*, **13**, 133–144..

— ,1956: The dynamic structure of a coastal plain estuary. *J. Mar. Res.*, **15**, 33–42..

— ,1967: Observations of circulation in coastal plain estuaries. *Estuaries*, Amer. Assoc. Advanc. Sci., 37–44..

Rattray, M., and D. V. Hansen, 1962: A similarity solution for the circulation in an estuary. *J. Mar. Res.*, **20**, 121–133..

Simpson, J. H., J. Brown, J. Matthews, and G. Allen, 1990: Tidal straining, density currents, and stirring in the control of estuarine stratification. *Estuaries*, **13**, 125–132..

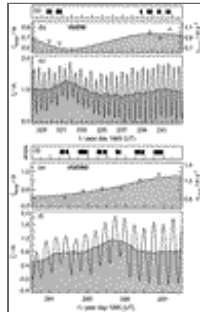
Thorpe, S. A., 1977: Turbulence and mixing in a Scottish loch. *Philos. Trans. Roy. Soc. London*, **286A**, 125–181..

Trowbridge, J. H., 1992: A simple description of the deepening and structure of a stably stratified flow driven by a surface stress. *J. Geophys. Res.*, **97**, 15 529–15 543..

— ,W. R. Geyer, M. M. Bowen, and A. J. Williams III, 1999: Near-bottom turbulence measurements in a partially mixed estuary: Turbulent energy balance, velocity structure, and along-channel momentum balance. *J. Phys. Oceanogr.*, **29**, 3056–3072.. [Find this article online](#)

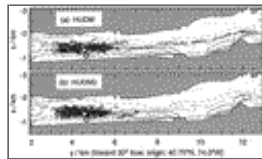
Yamazaki, H., and T. R. Osborn, 1993: Direct estimation of heat flux in the seasonal thermocline. *J. Phys. Oceanogr.*, **23**, 503–516.. [Find this article online](#)

Figures



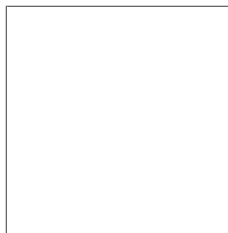
[Click on thumbnail for full-sized image.](#)

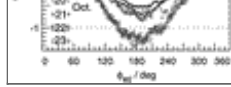
Fig. 1. Tides during HUDM and HUDM2. (a) and (d) Times of microstructure drops. (b) and (e) Amplitude of the tidal elevation at The Battery, New York City (shaded), and amplitude of depth-averaged tidal currents from the shipmounted ADCP (circles). (c) and (f) Actual water level at The Battery (solid line) and its low-pass filter (shaded). Labels of yeardays mark the beginning of the day in Universal Time [UT, (UTC)], local time plus 5 h.



[Click on thumbnail for full-sized image.](#)

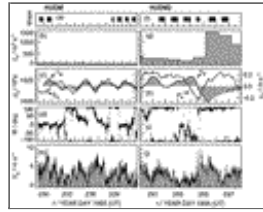
Fig. 2. Locations of microstructure drops during (a) cruise HUDM (Aug 1995) and (b) HUDM2 (Oct 1995) in the Hudson River off Manhattan. Isobaths are marked as follows: 6.1 m: dotted; 9.1 m: dashed; 12.2 m: dash-dotted; 15.2 m: solid; 18.3 m: dotted; 19.8 m: dash-dotted. The two large circles indicate the two central WHOI moorings, the bottom quadropod being closer to shore.





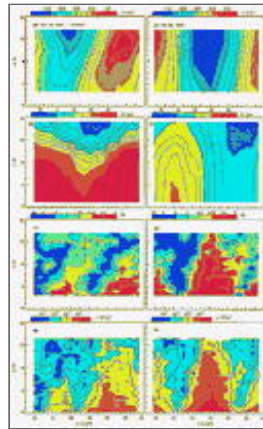
[Click on thumbnail for full-sized image.](#)

Fig. 3. Vertically averaged along-river currents from the shipmounted ADCP vs M_2 tidal phase as explained in the text.



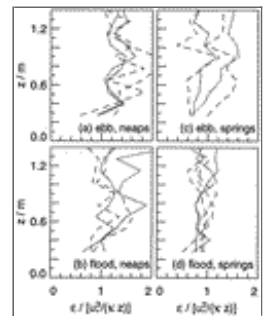
[Click on thumbnail for full-sized image.](#)

Fig. 4. Atmospheric forcing and river flow. (a) and (f) Times of microstructure drops. (b) and (g) River discharge (J_V) at Green Island, New York. Meteorological measurements at the 79th Street Marina. (c) and (h) Atmospheric pressure (p_a). (d) and (i) Wind direction (Φ). (e) and (j) Wind speed (V_a). Panels (c) and (h) also depict the low-passed, depth-averaged velocity from the central ADCP mooring (v_{lp} , shaded).



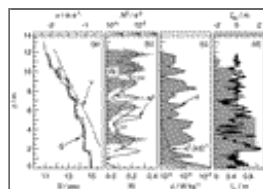
[Click on thumbnail for full-sized image.](#)

Fig. 5. Along-river currents, salinity, Richardson number, and viscous dissipation rate as function of time and height above bottom, cruise HUDM2, 19 Oct 1995 (yearday 292), representing neap tides, and 22 Oct (day 295), representing spring tides.



[Click on thumbnail for full-sized image.](#)

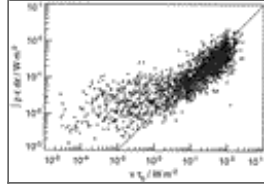
Fig. 6. Median of normalized dissipation rate ϵ/ϵ_b vs height above bottom; solid: HUDM2, dashed: HUDM, daily data as indicated.



[Click on thumbnail for full-sized image.](#)

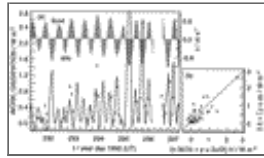
Fig. 7. Microstructure profile taken during spring tides with anomalously strong stratification showing vigorous mixing

throughout the water column, drop 6652, 23 Oct 1995 1901 UT (UTC). (a) Along-river velocity from the ADCP and salinity from the microstructure conductivity sensor (thick line, highly variable) as well as from the CTD, the latter Thorpe-sorted (thin line). (b) Squared buoyancy frequency from the regular CTD (thick) and from the microstructure T/C sensor (thin) as well as Richardson number from ADCP shear and CTD- N^2 (shaded). (c) Measured dissipation rate and dissipation rate expected from law-of-the-wall scaling. (d) Turbulent displacement (line) and Thorpe scale (shaded) based on the microstructure salinity.



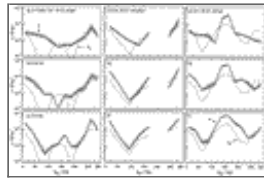
Click on thumbnail for full-sized image.

Fig. 8. Depth-integrated viscous dissipation rate from individual microstructure profiles extending to within 0.15 m off the bottom vs depth-averaged velocity times bottom shear stress estimated from 6-min ADCP averages (“+”—HUDM, “x”—HUDM2).



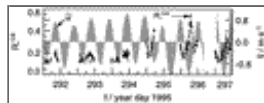
Click on thumbnail for full-sized image.

Fig. 9. Estuarine energy budget, cruise HUDM2: work done by the tidal pressure gradient adjusted for the rate of change kinetic energy (from moored observations by ADCP and pressure gauges—solid line), and depth-integrated dissipation rate from microstructure profiles multiplied by a factor of 2.5 (“x”). The depth-averaged streamwise velocity from the central mooring is also indicated (shaded).



Click on thumbnail for full-sized image.

Fig. 10. Dissipation rates as function of depth, phase of the semidiurnal tide, and progress from neap tides to spring tides, cruise HUDM2. The relationship between tidal phase ϕ_{M_2} and local tidal currents is depicted in [Fig. 3](#). The law-of-the-wall dissipation rate ϵ_b was computed from ADCP velocity data. Shading indicates statistical confidence limits.



Click on thumbnail for full-sized image.

Fig. 11. [Trowbridge's \(1992\)](#) criterion $R^{-1/4}$ for the extent of the wall layer relative to the water depth; depth-averaged velocity added for reference.

Corresponding author address: Dr. Hartmut Peters, Rosenstiel School of Marine and Atmospheric Science, University of Miami, 4600 Rickenbacker Causeway, Miami, FL 33149-1098.

E-mail: hpeters@rsmas.miami.edu



© 2008 American Meteorological Society [Privacy Policy and Disclaimer](#)

Headquarters: 45 Beacon Street Boston, MA 02108-3693

DC Office: 1120 G Street, NW, Suite 800 Washington DC, 20005-3826

amsinfo@ametsoc.org Phone: 617-227-2425 Fax: 617-742-8718

[Allen Press, Inc.](#) assists in the online publication of *AMS* journals.